

**Supplementary Information for:
High-Temperature Water Adsorption Isotherms and
Ambient Temperature Water Diffusion Rates
on Water Harvesting Metal-Organic Frameworks**

Jon Hastings¹, Thomas Lassitter¹, Zhiling Zheng², Saamil Chheda³, J. Ilja Siepmann³,
Laura Gagliardi⁴, Omar M. Yaghi², T. Grant Glover^{1,*}

1. Department of Chemical and Biomolecular Engineering, University of South Alabama,
2. Department of Chemistry, University of California, Berkeley
3. Department of Chemical Engineering and Materials Science,
Department of Chemistry and Chemical Theory Center,
University of Minnesota-Twin Cities, Minneapolis, MN 55455
4. Department of Chemistry, Pritzker School of Molecular Engineering,
Chicago Center for Theoretical Chemistry, University of Chicago,

*author to whom correspondence should be addressed

glover@southalabama.edu

1. Experimental

1.1 Breakthrough High-Temperature Water Adsorption Isotherms

A breakthrough system was constructed similar to Lassitter et al. (Figure S1)¹ where a glass tube of 1.5” inside diameter was loaded with 3.11 g sample and placed inside a Binder model MK240-400V environmental chamber to maintain temperatures ± 0.1 °C. A total flow of 200 ml min^{-1} of helium was delivered through MKS mass flow controllers and the gas was thermally equilibrated with the chamber temperature using a ¼ inch copper pipe as a heat exchanger. The length of pipe needed was determined by using a tube in shell and heat exchanger equation with only one tube with²

$$\dot{Q} = hA_{\delta}\Delta T_{lm} \quad (1)$$

Where \dot{Q} is the heat transfer rate, h is the heat transfer coefficient of the copper pipe, A_{δ} is the heat transfer area, and ΔT_{lm} is the log mean temperature difference. First, the heat transfer rate was determined by,

$$\dot{Q} = \dot{m}C_p\Delta T \quad (2)$$

where \dot{m} is the flowrate of the helium through the copper piping (0.595 g s^{-1}), C_p is the heat capacity of helium (5.193 $\text{J g}^{-1} \text{K}^{-1}$), and ΔT is the temperature difference between the incoming helium (25 °C) and the max temperature (100 °C) of the experiment. Equation 1 was then rearranged to determine the heat transfer area needed,

$$A_{\delta} = \frac{\dot{Q}}{h\Delta T_{lm}} \quad (3)$$

and the length of the pipe was determined by,

$$L = \frac{A_{\delta}}{\pi D} \quad (4)$$

where D is the diameter of the pipe.

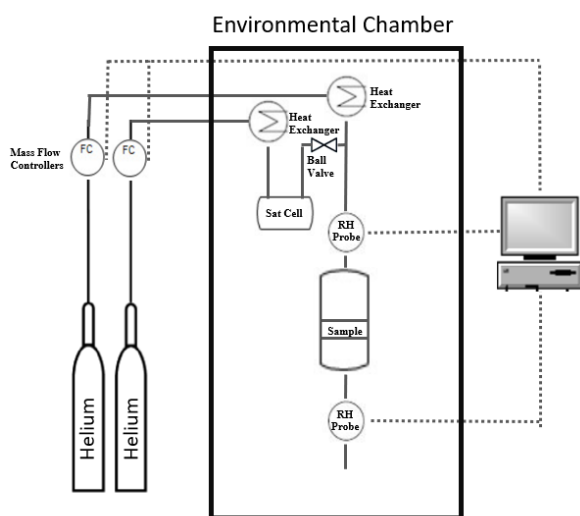


Figure S1. High-temperature breakthrough apparatus.

Based on Equation 4, it was determined that 4 feet of copper tubing was needed, but to ensure adequate thermal equilibrium, 6.5 feet of copper tubing was used on each incoming helium stream.

After reaching thermal equilibrium with the environmental chamber's internal temperature, one helium stream was passed through a triple-pass saturator cell filled with water to create specific humid conditions. The streams were then merged into one stream, where the relative humidity was recorded before and after contacting the sample using a Honeywell HIH-4020-001 relative humidity probe with a known humidity error of 3.5%. The relative humidity (RH) data acquisition was completed using LabVIEW via USB-6003-NI device at one data point per minute

sampling rate.

Similar to previously reported breakthrough results,³⁻⁹ the data were used to calculate the capacity using the following equations. First, a concentration-time (Ct) number was defined as

$$Ct_{feed} = t_f C_{feed} \quad (5)$$

where Ct_{feed} has units of RH*s, t_f is the time the feed is passed to the system, and C_{feed} is the concentration of the feed in RH. The Ct eluting from the sorbent until feed termination is integrated under the elution curve, using the midpoint rule,

$$Ct_{elution} = \sum_{t=0}^{t_s} \frac{C_n + C_{n-1}}{2} (t_n - t_{n-1}) \quad (6)$$

where $Ct_{elution}$ has units of RH * s, t_s is the time to saturation in seconds, C_n is the concentration at time n in RH, and C_{n-1} is the concentration at time $n - 1$ in RH.⁹

1.2 Volumetric High-Temperature Water Adsorption Isotherms

A volumetric apparatus was constructed similar to that of Rudisill et al. Shown in Figure S2.¹⁰ The apparatus was placed inside of an environmental chamber able to maintain temperatures ± 0.1 °C to ensure thermal stability. HPLC grade liquid water, sourced from Sigma-Aldrich SHBP9108, was injected through an injection port in the loop. The resulting pressure was recorded using a 1000 mmHg National Institute of Standards and Technology (NIST) traceable, heated capacitance-manometer from MKS Instruments, Inc., accurate to 0.01% of full scale and 0.5% of the indicated value. A leak rate of 1×10^{-4} torr in 24 hrs was measured to ensure that the moles of gas that leaked into the system were negligible.

The volumetric measurements are based on a mass balance requiring precise apparatus volume measurements. Therefore, a helium expansion technique was used where the volume was determined using a calibrated cylinder of a known volume and two (NIST) traceable, heated, capacitance-manometers from MKS Instruments accurate to 0.01% of full scale and 0.5% of the indicated value. With the system volumes known, a sample of approximately 200-300 mg of adsorbent measured on a balance with an accuracy of 0.1 mg up to 220 g was inserted into the adsorbent bed. Pressure readings before and after exposure to the adsorbent were recorded using LabVIEW.

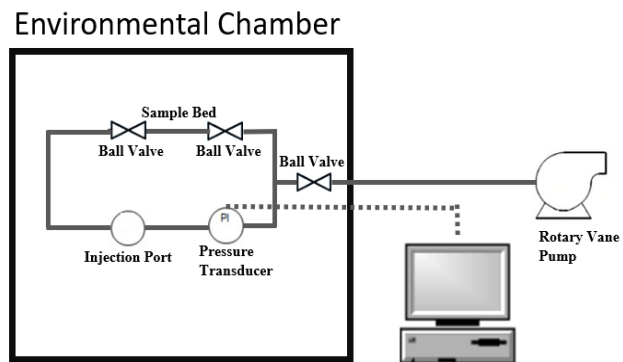


Figure S2. High temperature water adsorption isotherm apparatus.

1.3 Single Component Adsorption Isotherms

Before collecting elevated-temperature water adsorption data, single-component adsorption data was collected using a Micromeritics 3 Flex and Micromeritics 2020 at 25 °C, as shown in Figure S3.

1.4 Isothermic Heats of Adsorption

The isosteric heat of water adsorption was calculated, using a temperature range from 45 °C to 115 °C in 10-degree increments, by the Clausius–Clapeyron equation,

$$\ln(P) = \frac{\Delta H_{ads}}{R} \left(\frac{1}{T} \right) \quad (7)$$

where P is pressure, R is the gas constant, and T is the temperature in Kelvin, by first fitting the loading of each water adsorption curve using linear interpolation and then iterating on pressure using a sum squared method to obtain the corresponding pressure values at specific loadings.¹¹ The natural log of the obtained pressure was then plotted against the inverse of temperature. The enthalpy of adsorption was then calculated by taking the slope at each loading and multiplying by R , where the slope equals,

$$\frac{d\ln(P)}{d\left(\frac{1}{T}\right)} \quad (8)$$

and the data is then plotted at each loading.^{11,12}

The error reported in Table 1 was calculated based on the 0.5% of the indicated value from the (NIST) traceable, heated, capacitance-manometers from MKS Instruments. The error for each pressure reading at each loading, and for each temperature, was introduced to the calculations shown in eq 7 and is reported as the standard error of the mean. To be conservative the largest error for each sample, found at the lowest loading for each sample, was reported in Table 1.

1.5 Simulated Isothermic Heats of Adsorption

Isobaric-isothermal (NpT) Gibbs ensemble Monte Carlo (GEMC) simulations were performed on a rigid framework structure of MOF-303 to simulate the water adsorption isotherms at 45 °C and 85 °C using a similar setup as previously used by Chheda et al.¹³ Pairwise Lennard-Jones and Coulomb interactions within a spherical cutoff of 14 Å were included. Analytical tail corrections for the LJ interactions and the Ewald summation method for the electrostatic interactions were

used for interactions beyond the spherical cutoff of 14 Å. The ‘FF3’ force field parameters used previously by Chheda et al. were employed in this work.¹³ The Lorentz-Berthelot mixing rules were used for describing the MOF-water interactions.

The isosteric heat of water adsorption, Q_{st} , was computed from the fluctuations in the potential energy of the adsorbed phase and adsorbed water loading using

$$-Q_{st} = \frac{\langle U_a N_a \rangle - \langle U_a \rangle \langle N_a \rangle}{\langle N_a^2 \rangle - \langle N_a \rangle^2} - \frac{\langle U_g \rangle + p \langle V_g \rangle}{\langle N_g \rangle} \quad (9)$$

where U_a is the potential energy of the adsorbed phase comprising adsorbate–adsorbate and adsorbate–framework interactions, and N_a is the loading of adsorbed molecules in the MOF. Similarly, U_g and N_g are the potential energy and the number of adsorbate molecules in the reservoir phase, respectively.

1.6 Kinetic Data

The concentration swing frequency response (CSFR) measurements were completed using a system similar to the one used by Glover et al.^{14,15} Briefly, helium was passed through a water saturator cell that was located in a temperature-controlled water bath, allowing for gas phase water concentrations to be controlled by setting the water bath temperature. The pressure was controlled at 50 torr above atmospheric pressure using a pressure controller (MKS Baratron type 640B) upstream of the saturator. A second helium stream was mixed with the adsorbate feed stream prior to the adsorbent bed. Both streams were controlled using MKS mass flow controllers and the adsorbate gas concentration fed to the adsorbent bed was determined by the combined flow rates of the two streams. An Agilent 5973 mass spectrometer sampled the effluent gas from the adsorbent bed.

Dry weights were determined by weighing the empty bed and loading a sample into the sample bed, followed by degassing in situ. The sample loaded bed was weighted after degassing, and the sample mass was determined by the difference in mass.

After regeneration, the bed was reinserted into the CSFR and exposed to a constant, unperturbed feed of water in helium at the selected humidity overnight to equilibrate the bed at the selected water loading. Next, the flow rates of the two helium streams were perturbed sinusoidally at a selected frequency, with each stream 180 degrees out of phase relative to the other. The resulting feed stream to the adsorbent bed had a constant total flow rate with a sinusoidal adsorbate concentration oscillating around the equilibrium state. To maintain the linearity of the system, the amplitude of the perturbations for both streams were kept small. Specifically, the swing used in this work was ± 0.4 sccm on each stream. In this work, CSFR experiments were conducted over a frequency range of 0.0001 to 1 Hz. Unless noted otherwise, all measurements were performed at 25 (± 1 °C).

The Darken equation was used to correlate diffusivity from gathered micropore diffusion rates with sorbate concentration, as shown below:

$$D = D_o \frac{d \ln(p)}{d \ln(c)} \quad (7)$$

where D_o is the corrected diffusivity and $\frac{d \ln(p)}{d \ln(c)}$ is the thermodynamic correction factor. It was assumed that the corrected diffusivity was independent of loading. The correction factor was calculated from the isotherm data at 25 °C by utilizing a linear interpolation of the isotherm slope.^{16,17}

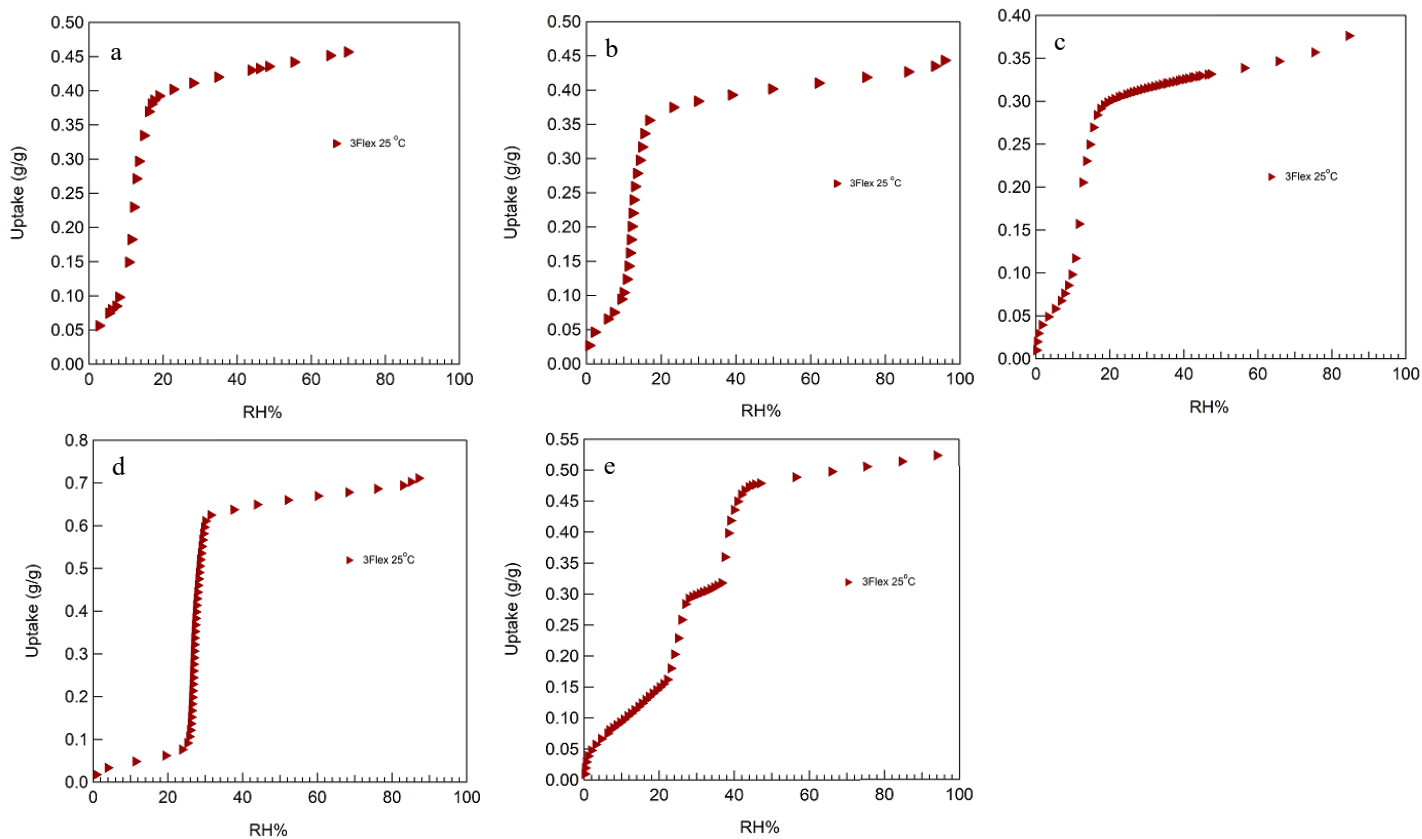


Figure S3. (a) 25 °C water adsorption isotherms collected on a micromeritics 3Flex for novoMOF MOF-303, (b) MOF-303, (c) Framergy MOF-303, (d) LA2-1, (e) MIL-100(Fe).

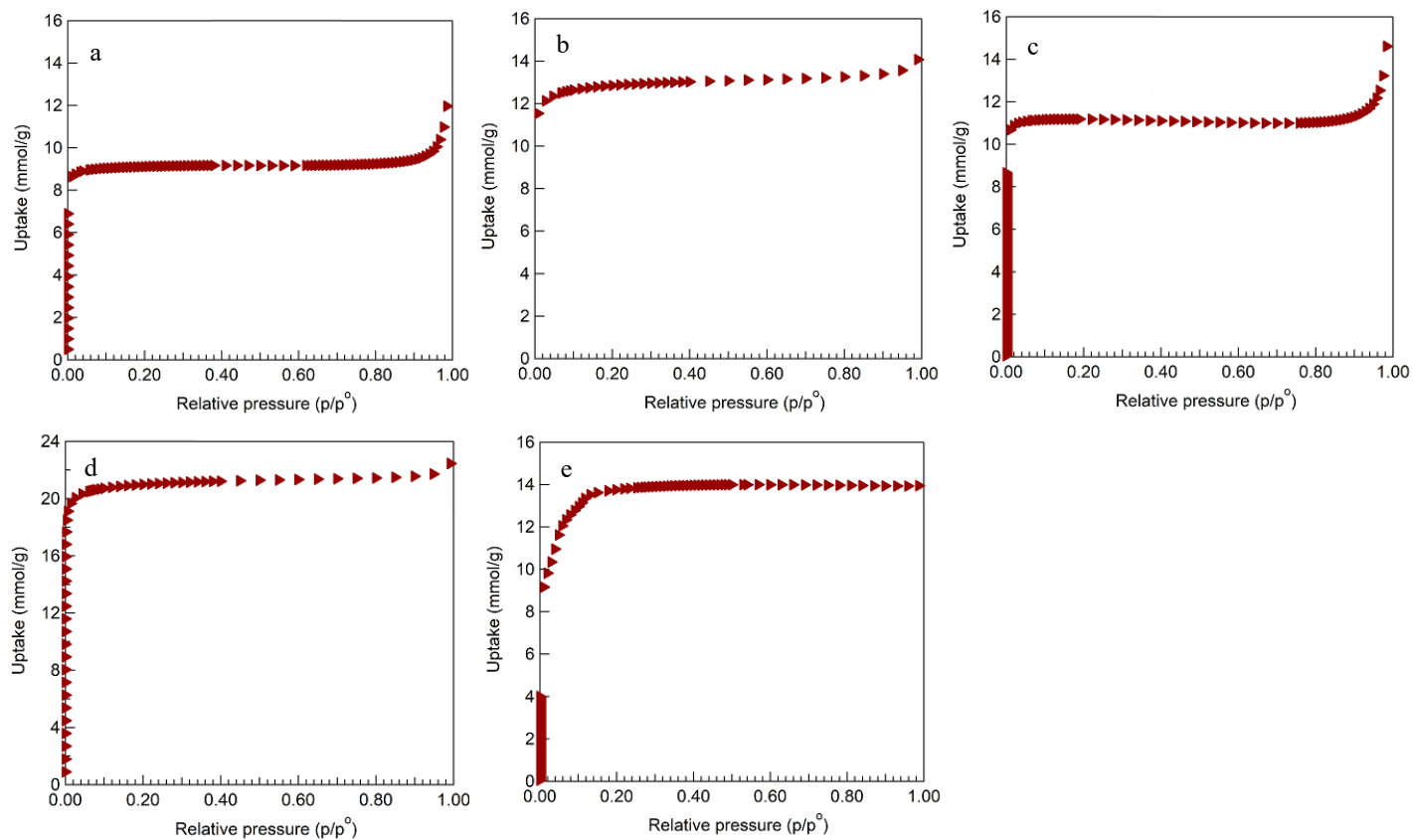


Figure S4. (a) Nitrogen adsorption isotherms measured at 77 K collected on a Micromeritics 3Flex for novoMOF MOF-303 (BET surface area 837.24 m²/g), (b) MOF-303 (BET surface area 1268.07 m²/g), (c) Framergy MOF-303 (BET surface area 1039.10 m²/g), (d) MOF-LA2-1 (BET surface area 1894.66 m²/g), (e) MIL-100(Fe) (BET surface area 1134.36 m²/g).

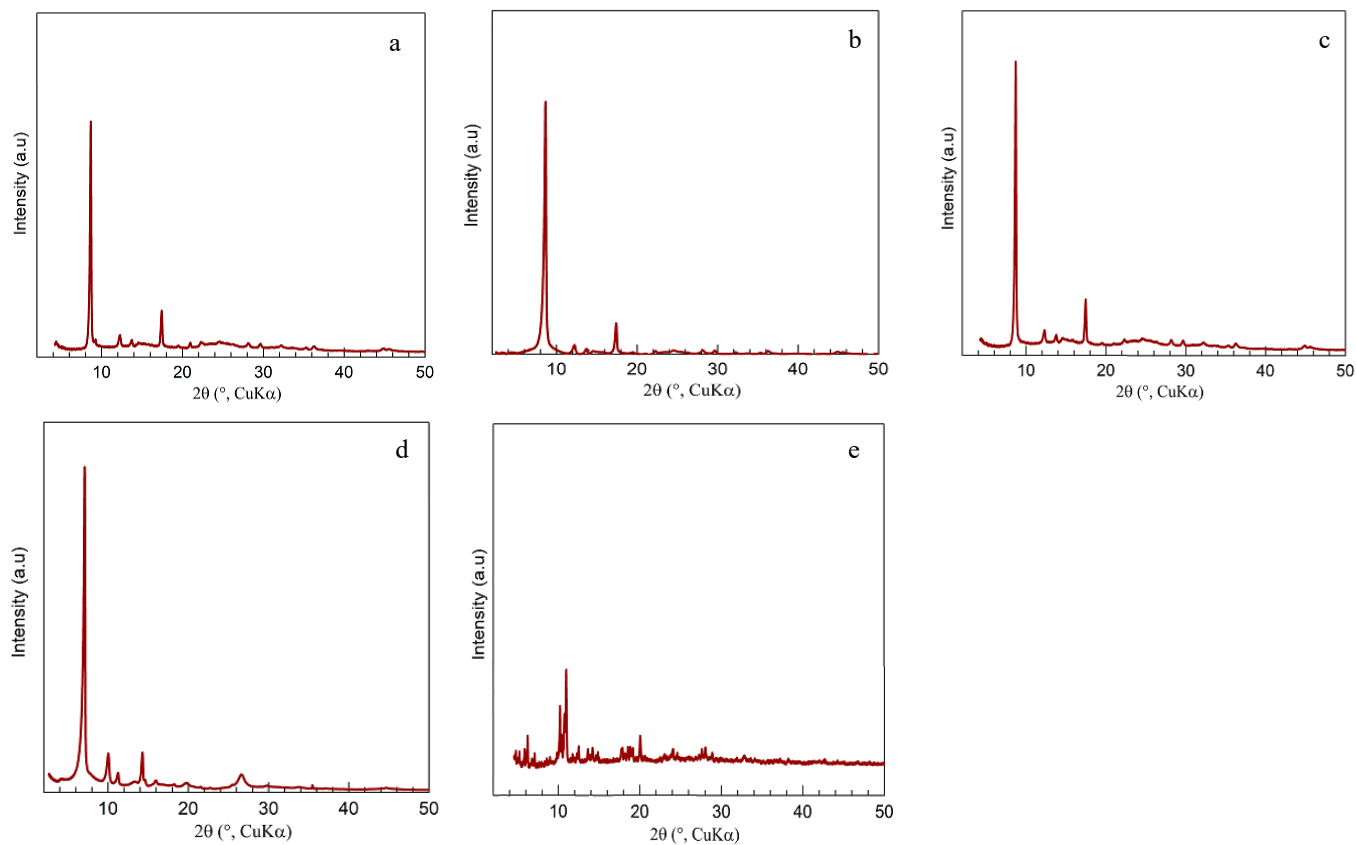


Figure S5. (a) PXRD patterns for novoMOF MOF-303, (b) MOF-303, (c) Framergy MOF-303, (d) MOF-LA2-1, (e) MIL-100(Fe).

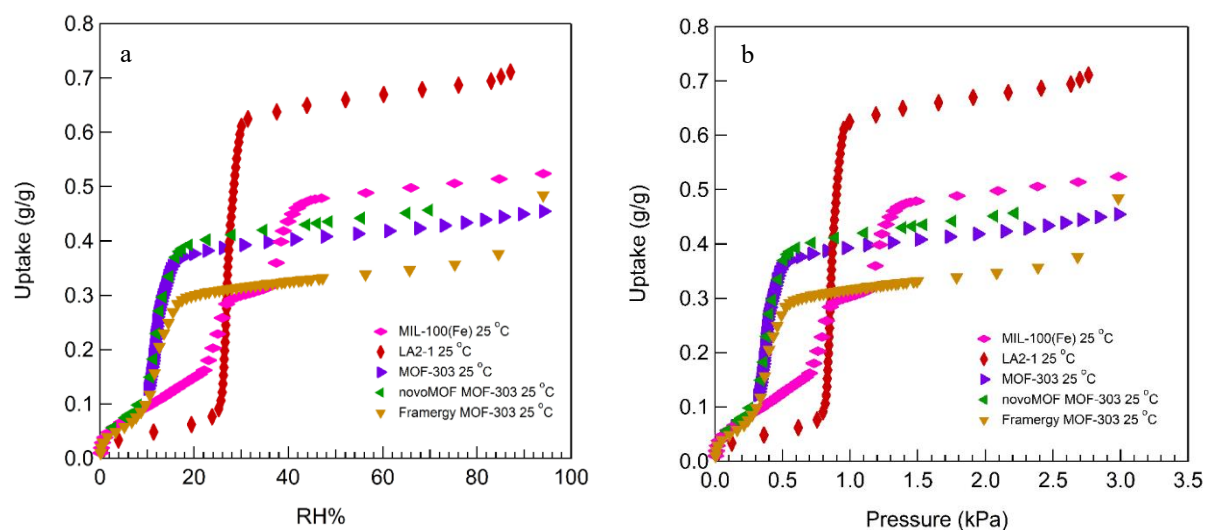


Figure S6. (a) 25°C water adsorption isotherms comparisons shown as RH% and (b) kPa to illustrate the differences in adsorption.

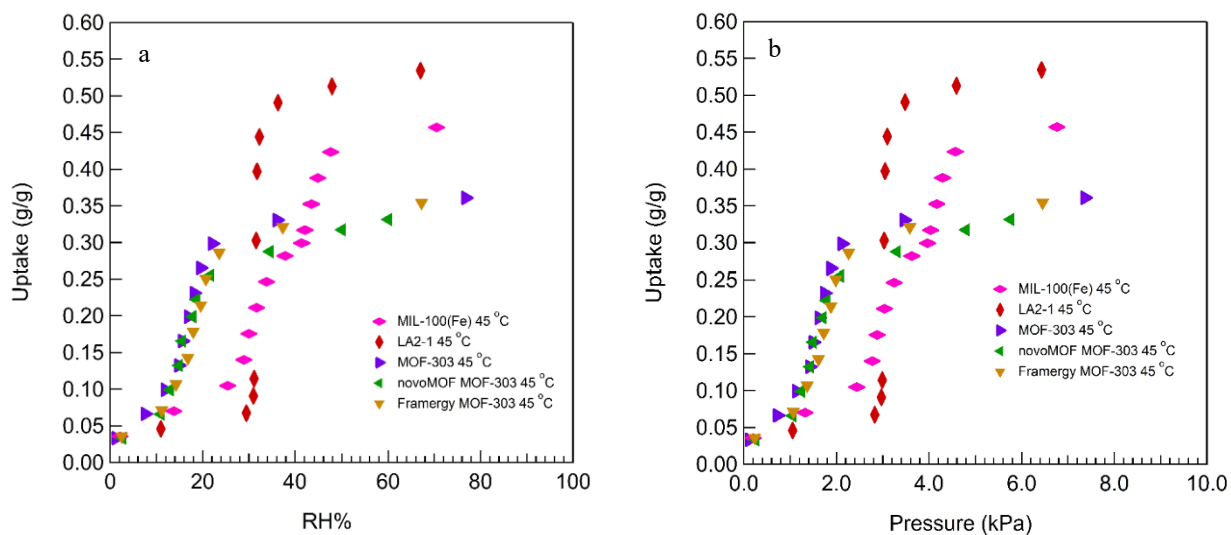


Figure S7. (a) 45 °C water adsorption isotherms comparisons shown as RH% and (b) kPa to illustrate the differences in adsorption.

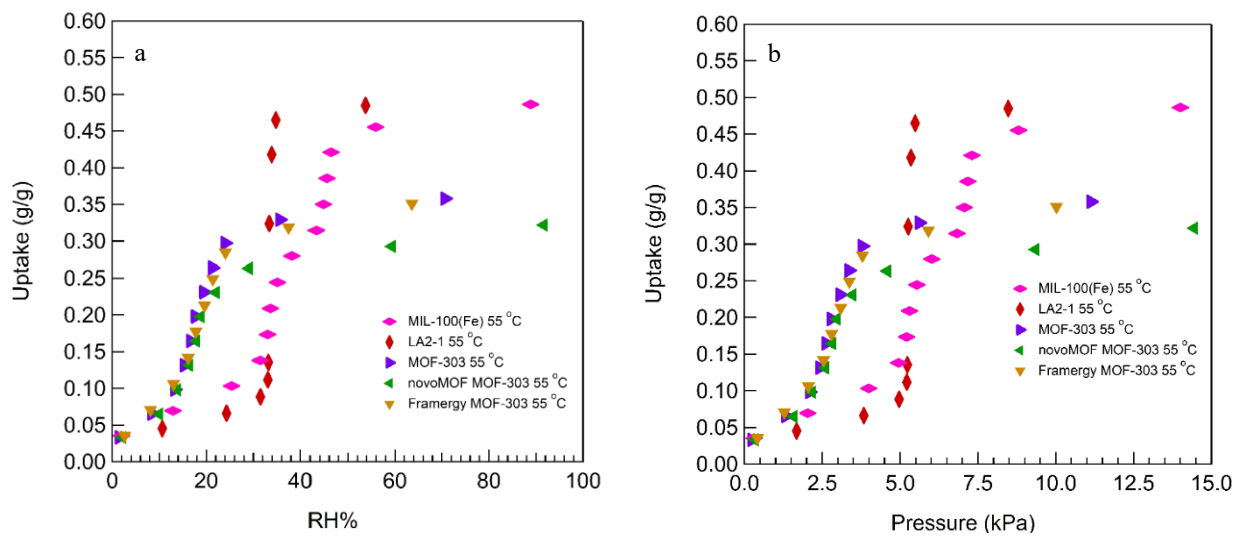


Figure S8. (a) 55 °C water adsorption isotherms comparisons shown as RH% and (b) kPa to illustrate the differences in adsorption.

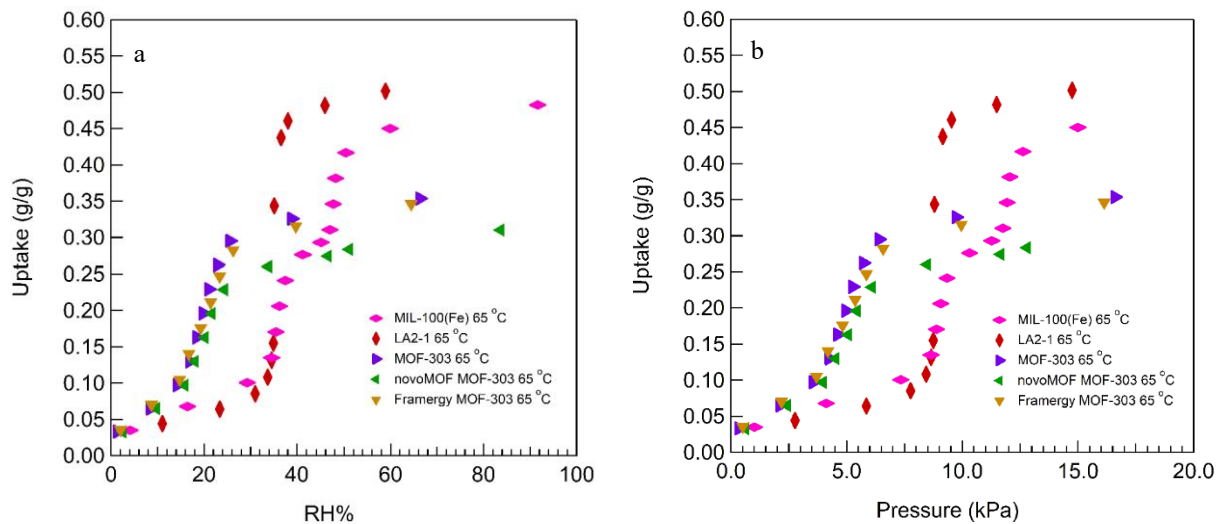


Figure S9. (a) 65 °C water adsorption isotherms comparisons shown as RH% and (b) kPa to illustrate the differences in adsorption.

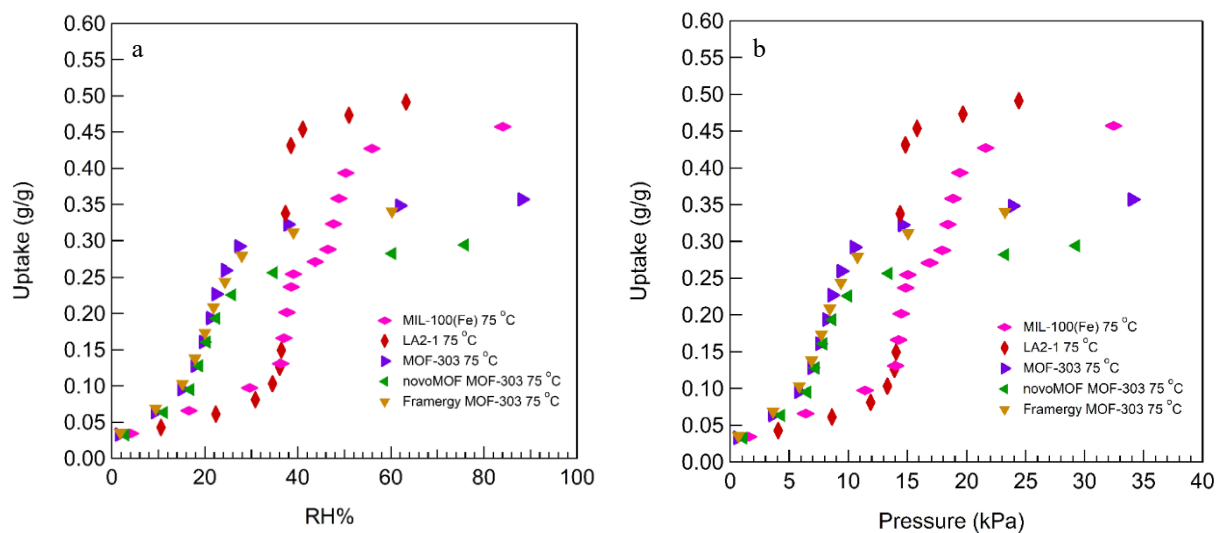


Figure S10. (a) 75 °C water adsorption isotherms comparisons shown as RH% and (b) kPa to illustrate the differences in adsorption.

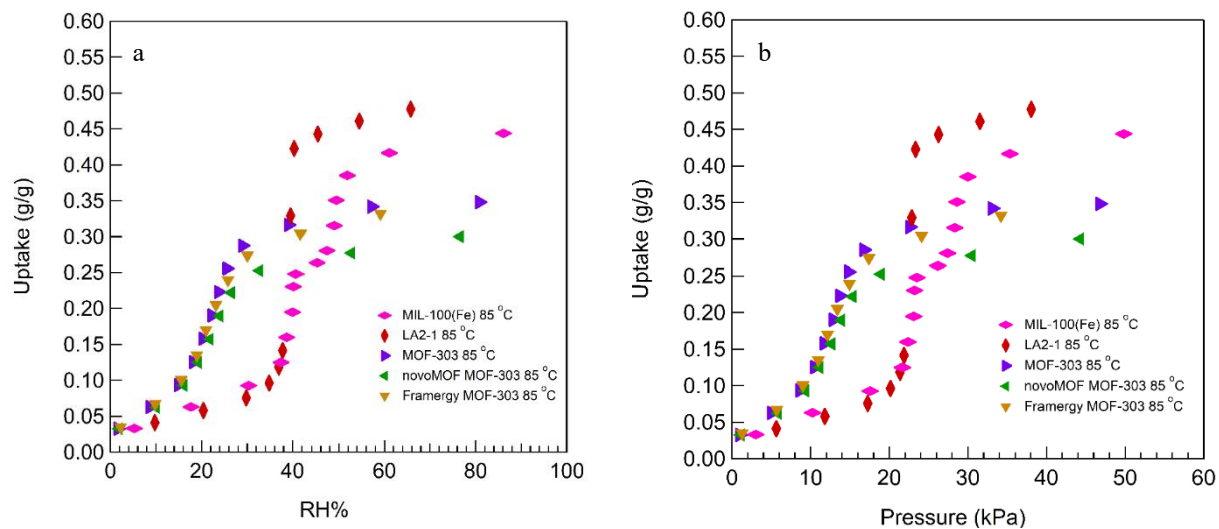


Figure S11. (a) 85 °C water adsorption isotherms comparisons shown as RH% and (b) kPa to illustrate the differences in adsorption.

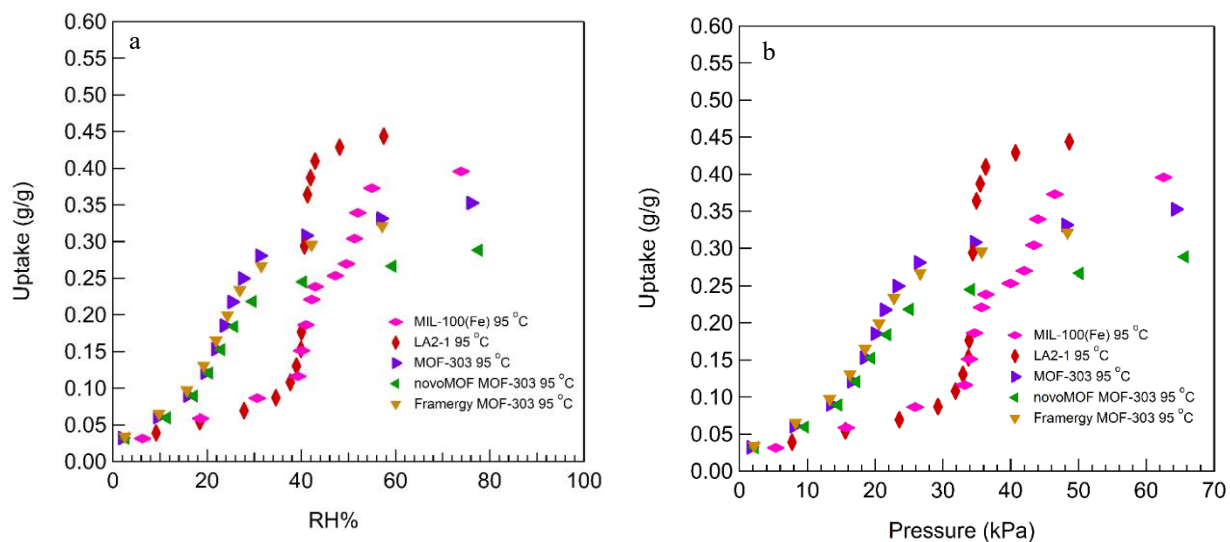


Figure S12. (a) 95 °C water adsorption isotherms comparisons shown as RH% and (b) kPa to illustrate the differences in adsorption.

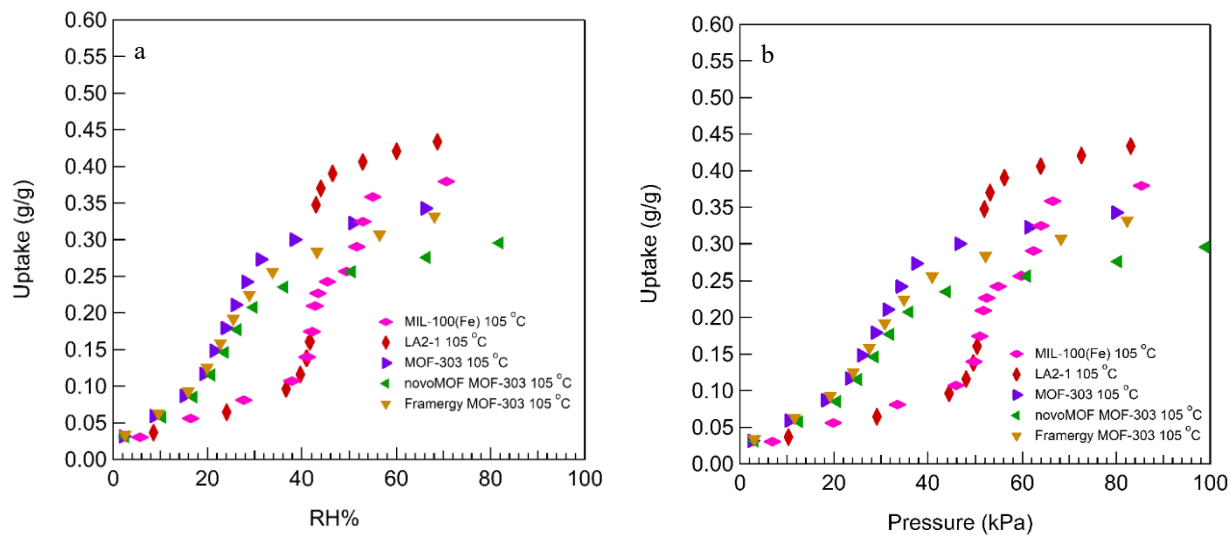


Figure S13. (a) 105 °C water adsorption isotherms comparisons shown as RH% and (b) kPa to illustrate the differences in adsorption.

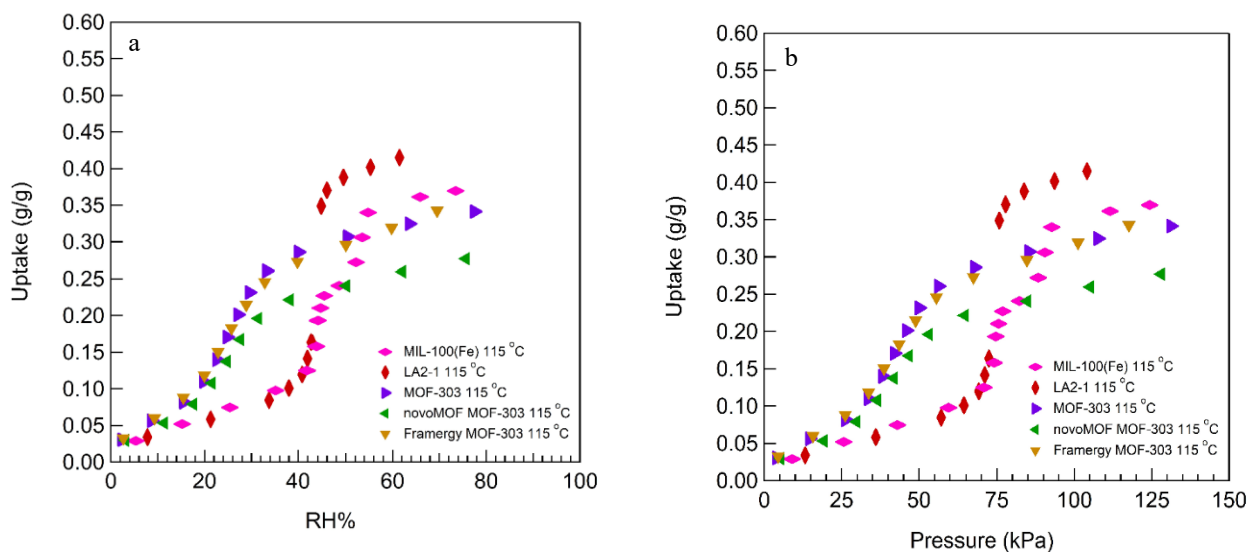


Figure S14. (a) 115 °C water adsorption isotherms comparisons shown as RH% and (b) kPa to illustrate the differences in adsorption.

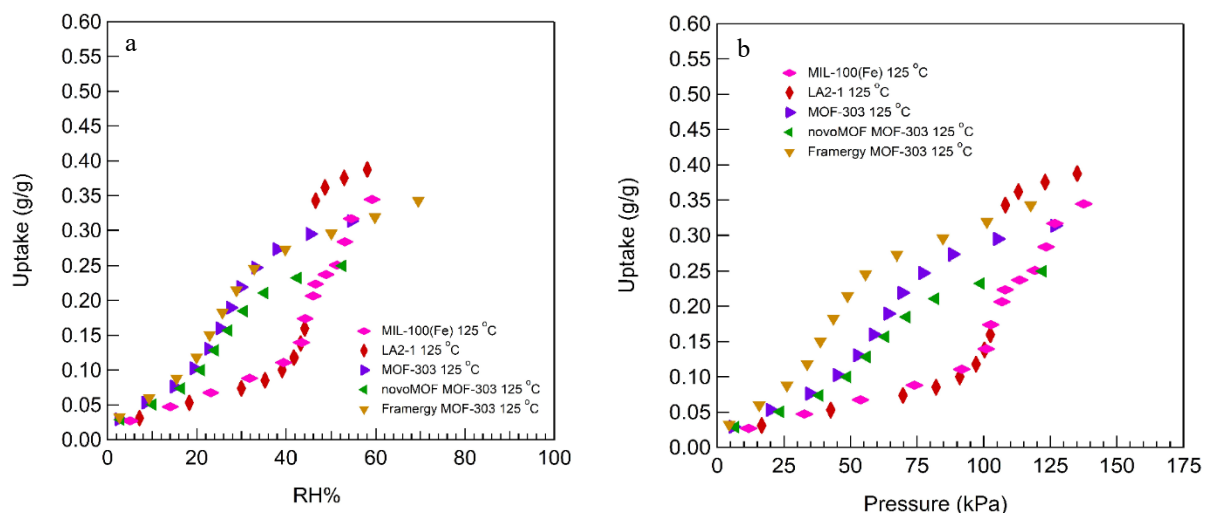


Figure S15. (a) 125 °C water adsorption isotherms comparisons shown as RH% and (b) kPa to illustrate the differences in adsorption.

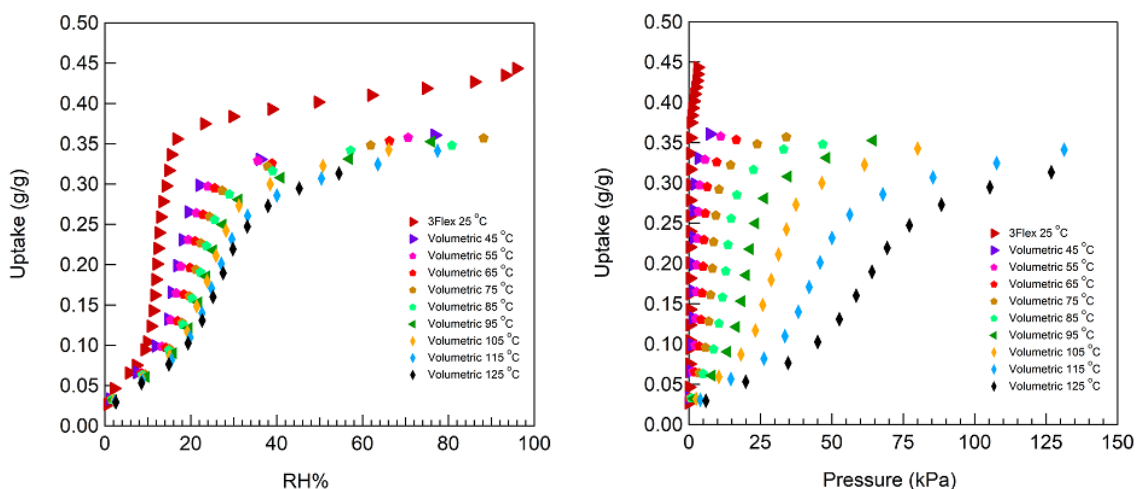


Figure S16. (a) Elevated temperature adsorption isotherms on MOF-303 from 25 °C to 125 °C represented in relative humidity and (b) kPa. This is the same data set as shown in manuscript Figure 2.

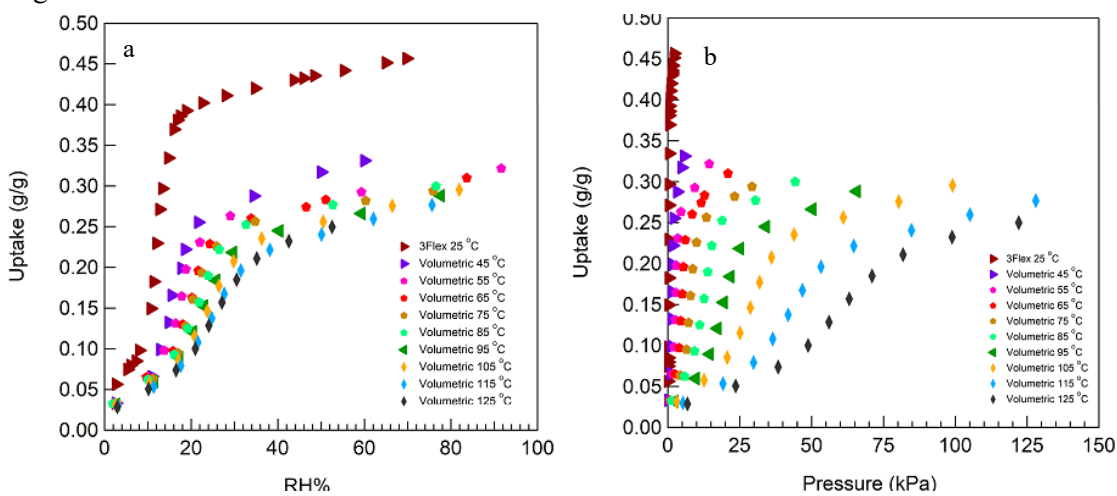


Figure S17. (a) Elevated temperature adsorption isotherms on MOF-303 supplied by novoMOF from 25 °C to 125 °C represented in relative humidity and (b) kPa.

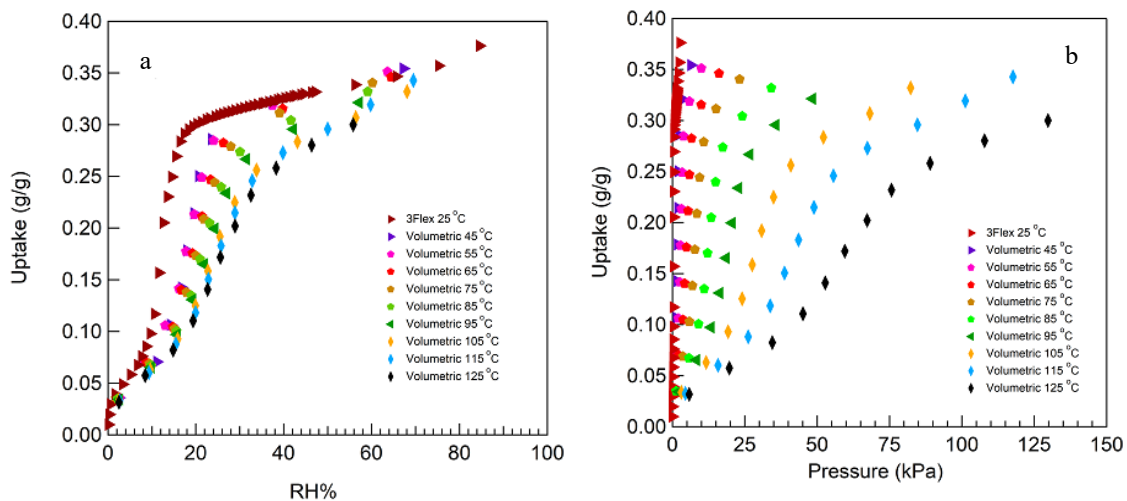


Figure S18. (a) Elevated temperature adsorption isotherms on Framergy MOF-303 from 25 °C to 125 °C represented in relative humidity and (b) kPa.

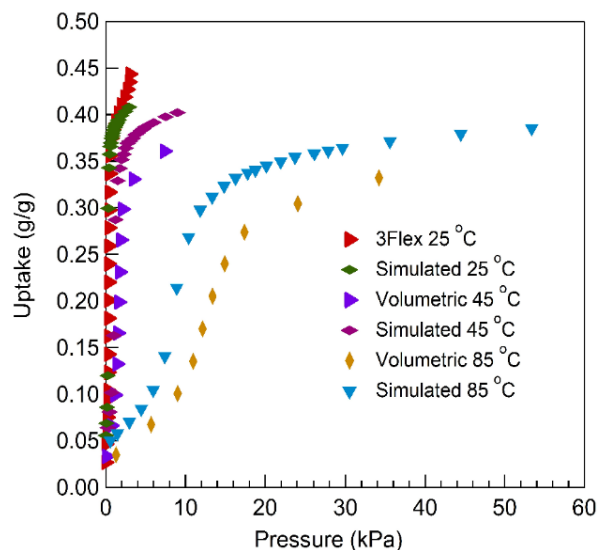


Figure S19. (a) Comparison of MOF-303 water isotherms and water isotherms collected using GEMC simulations in kPa

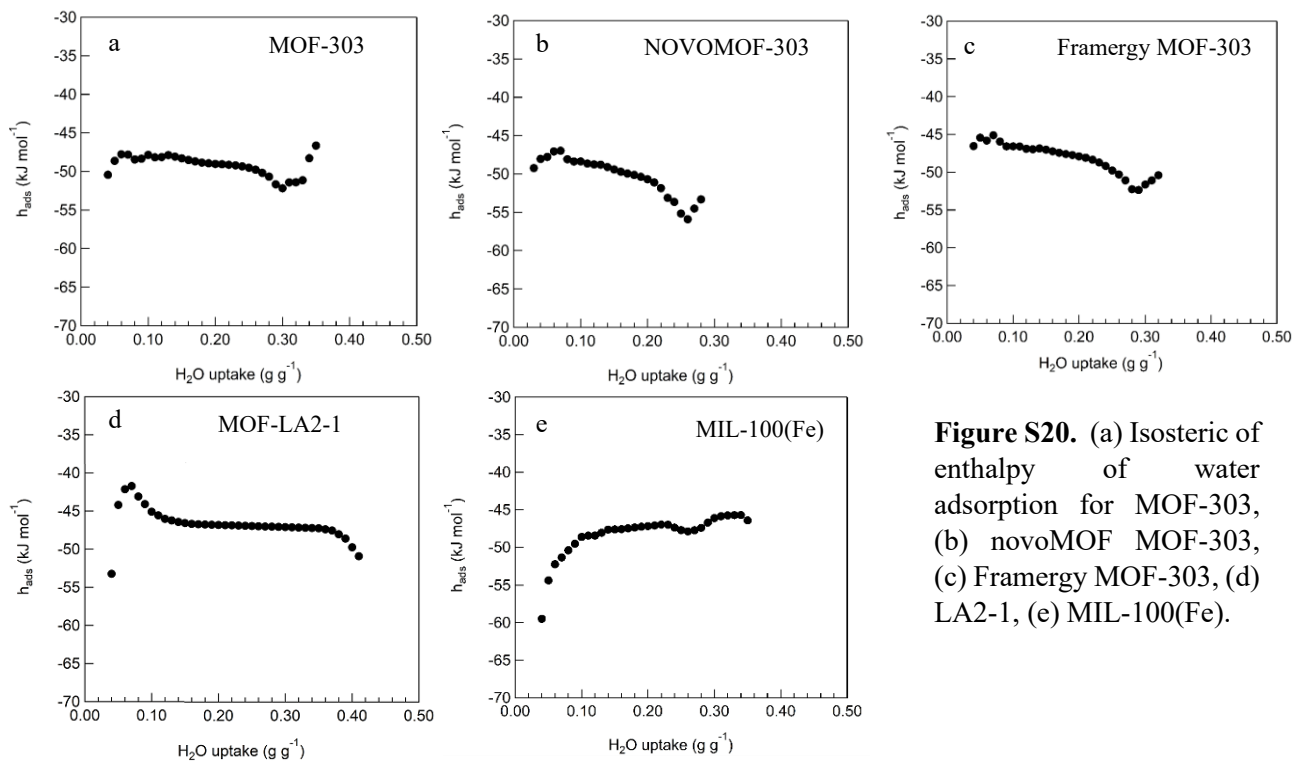


Figure S20. (a) Isothermic of enthalpy of water adsorption for MOF-303, (b) novoMOF MOF-303, (c) Framergy MOF-303, (d) LA2-1, (e) MIL-100(Fe).

2.0 Simulation Details

Table S1: Site occupancies of different framework adsorption sites in MOF-303 upon water adsorption at different temperatures and at $RH = 0.025$. A distance-based criterion was used to compute the water-MOF interactions.

| H-bonding functionalities | | | Site occupancies per unit cell | | | | | |
|---|---------------------|------------------|--------------------------------|------|-------|------|-------|------|
| $N(H)_{\text{linker}}$ | N_{linker} | O_{rod} | 25 °C | | 45 °C | | 85 °C | |
| <i>Primary patch in the strongly hydrophilic region</i> | | | | | | | | |
| yes | yes | yes | 3.96 | 4.14 | 3.94 | 4.15 | 3.88 | 4.15 |
| yes | yes | no | 0.04 | | 0.05 | | 0.10 | |
| yes | no | yes | 0.11 | | 0.11 | | 0.11 | |
| yes | no | no | 0.01 | | 0.02 | | 0.02 | |
| no | yes | yes | 0.00 | | 0.01 | | 0.01 | |
| no | yes | no | 0.02 | | 0.02 | | 0.03 | |
| <i>Secondary patch in the strongly hydrophilic region</i> | | | | | | | | |
| yes | yes | yes | 0.00 | 1.75 | 0.00 | 1.37 | 0.00 | 0.81 |
| yes | yes | no | 0.98 | | 0.70 | | 0.38 | |
| yes | no | yes | 0.00 | | 0.00 | | 0.00 | |
| yes | no | no | 0.03 | | 0.04 | | 0.03 | |
| no | yes | yes | 0.00 | | 0.00 | | 0.00 | |
| no | yes | no | 0.74 | | 0.63 | | 0.40 | |
| <i>Other</i> | | | | | | | | |
| no | no | yes | 0.05 | 0.05 | 0.05 | 0.05 | 0.05 | 0.05 |
| no | no | no | 0.04 | 0.04 | 0.06 | 0.06 | 0.06 | 0.06 |
| Total | | | 5.98 | | 5.63 | | 5.07 | |

Table S2: Site occupancies of different framework adsorption sites in MOF-303 upon water adsorption at different temperatures and at $RH = 0.051$. A distance-based criterion was used to compute the water-MOF interactions.

| H-bonding functionalities | | | Site occupancies per unit cell | | | | | |
|---|---------------------|------------------|--------------------------------|------|-------|------|-------|------|
| $N(H)_{\text{linker}}$ | N_{linker} | O_{rod} | 25 °C | | 45 °C | | 85 °C | |
| <i>Primary patch in the strongly hydrophilic region</i> | | | | | | | | |
| yes | yes | yes | 3.96 | 4.45 | 3.95 | 4.42 | 3.91 | 4.32 |
| yes | yes | no | 0.05 | | 0.07 | | 0.09 | |
| yes | no | yes | 0.32 | | 0.27 | | 0.21 | |
| yes | no | no | 0.05 | | 0.05 | | 0.04 | |
| no | yes | yes | 0.01 | | 0.01 | | 0.01 | |
| no | yes | no | 0.06 | | 0.07 | | 0.06 | |
| <i>Secondary patch in the strongly hydrophilic region</i> | | | | | | | | |
| yes | yes | yes | 0.00 | 2.76 | 0.00 | 2.36 | 0.00 | 1.58 |
| yes | yes | no | 1.42 | | 1.16 | | 0.70 | |
| yes | no | yes | 0.00 | | 0.00 | | 0.00 | |
| yes | no | no | 0.07 | | 0.07 | | 0.06 | |
| no | yes | yes | 0.00 | | 0.00 | | 0.00 | |
| no | yes | no | 1.27 | | 1.13 | | 0.82 | |
| <i>Other</i> | | | | | | | | |
| no | no | yes | 0.11 | 0.11 | 0.11 | 0.11 | 0.11 | 0.11 |
| no | no | no | 0.24 | 0.24 | 0.22 | 0.22 | 0.19 | 0.19 |
| Total | | | 7.56 | | 7.11 | | 6.2 | |

Table S3: Site occupancies of different framework adsorption sites in MOF-303 upon water adsorption at different temperatures and at $RH = 0.205$. A distance-based criterion was used to compute the water-MOF interactions.

| H-bonding functionalities | | | Site occupancies per unit cell | | | | | |
|---|---------------------|------------------|--------------------------------|-------|-------|-------|-------|-------|
| $N(H)_{\text{linker}}$ | N_{linker} | O_{rod} | 25 °C | | 45 °C | | 85 °C | |
| <i>Primary patch in the strongly hydrophilic region</i> | | | | | | | | |
| yes | yes | yes | 4.09 | 8.34 | 4.08 | 8.28 | 4.03 | 7.84 |
| yes | yes | no | 0.12 | | 0.12 | | 0.16 | |
| yes | no | yes | 1.64 | | 1.62 | | 1.42 | |
| yes | no | no | 0.80 | | 0.81 | | 0.81 | |
| no | yes | yes | 0.01 | | 0.01 | | 0.02 | |
| no | yes | no | 1.68 | | 1.64 | | 1.40 | |
| <i>Secondary patch in the strongly hydrophilic region</i> | | | | | | | | |
| yes | yes | yes | 0.00 | 7.07 | 0.00 | 6.9 | 0.00 | 6.08 |
| yes | yes | no | 1.79 | | 1.58 | | 1.25 | |
| yes | no | yes | 0.00 | | 0.00 | | 0.00 | |
| yes | no | no | 1.11 | | 1.22 | | 1.10 | |
| no | yes | yes | 0.00 | | 0.00 | | 0.00 | |
| no | yes | no | 4.17 | | 4.10 | | 3.73 | |
| <i>Other</i> | | | | | | | | |
| no | no | yes | 1.65 | 1.65 | 1.50 | 1.50 | 1.30 | 1.30 |
| no | no | no | 15.47 | 15.47 | 14.24 | 14.24 | 10.94 | 10.94 |
| Total | | | 32.53 | | 30.92 | | 26.16 | |

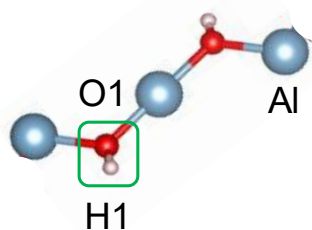
Table S4: Numerical data for water adsorption isotherms in MOF-303 obtained using NpT -GEMC simulations at $T = 45\text{ }^\circ\text{C}$ and $T = 85\text{ }^\circ\text{C}$. The vapor pressure of water using the TIP4P model is $13.747 \pm 0.043\text{ kPa}$ at $45\text{ }^\circ\text{C}$ and $82.061 \pm 0.218\text{ kPa}$ at $85\text{ }^\circ\text{C}$ respectively. The water loading is reported as molecules per unit cell, where the uncertainty in the last digits is denoted in the subscript.

| $T = 45\text{ }^\circ\text{C}$ | | $T = 85\text{ }^\circ\text{C}$ | |
|--------------------------------|---------------------|--------------------------------|---------------------|
| <i>RH</i> | Water uptake | <i>RH</i> | Water uptake |
| - | - | 0.010 | 4.419 ₂ |
| 0.025 | 5.62 ₁ | 0.025 | 5.08 ₁ |
| 0.052 | 7.11 ₂ | 0.051 | 6.19 ₁ |
| 0.078 | 8.94 ₉ | 0.077 | 7.40 ₂ |
| 0.104 | 14.34 ₃₁ | 0.103 | 9.19 ₅ |
| 0.130 | 25.26 ₁₉ | 0.128 | 12.39 ₁₃ |
| 0.156 | 28.93 ₈ | 0.154 | 18.83 ₂₀ |
| 0.183 | 30.09 ₂ | 0.180 | 23.62 ₉ |
| 0.208 | 30.92 ₇ | 0.205 | 26.18 ₆ |
| 0.234 | 31.42 ₅ | 0.231 | 27.43 ₆ |
| 0.261 | 32.03 ₆ | 0.256 | 28.46 ₅ |
| 0.286 | 32.47 ₆ | 0.281 | 29.19 ₄ |
| 0.312 | 32.67 ₆ | 0.307 | 29.68 ₆ |
| - | - | 0.324 | 29.97 ₅ |
| 0.354 | 32.93 ₃ | 0.348 | 30.36 ₅ |
| 0.385 | 33.26 ₆ | 0.379 | 30.75 ₄ |
| 0.417 | 33.43 ₃ | 0.410 | 31.17 ₃ |
| 0.458 | 33.68 ₄ | 0.451 | 31.53 ₅ |
| 0.489 | 33.84 ₃ | 0.481 | 31.78 ₅ |
| 0.520 | 34.03 ₂ | 0.512 | 32.06 ₄ |
| 0.625 | 34.43 ₂ | 0.615 | 32.66 ₃ |
| 0.781 | 34.96 ₆ | 0.768 | 33.36 ₄ |
| 0.937 | 35.36 ₅ | 0.922 | 33.90 ₄ |

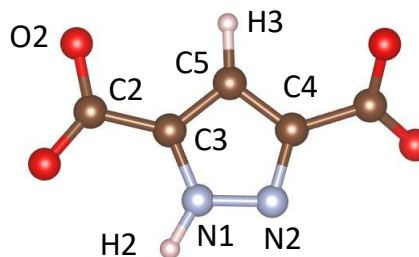
Table S5: Lennard-Jones parameters and partial charges used to describe the interactions of MOF-303 with the framework.

| Atom type | $\epsilon / k_B(\text{K})$ | $\sigma(\text{\AA})$ | q (e) |
|-----------|----------------------------|----------------------|-----------|
| Al | 254.00 | 4.000 | 1.64 |
| O1 | 30.19 | 3.118 | -0.98 |
| H1 (FF1) | 22.14 | 2.571 | 0.43 |
| H1 (FF2) | 0.05 | 2.846 | 0.43 |
| H1 (FF3) | 0.00 | 0.000 | 0.43 |
| O2 | 79.00 | 3.050 | -0.57 |
| C2 | 41.00 | 3.900 | 0.704 |
| C3 | 30.70 | 3.600 | 0.081 |
| N1 | 141.00 | 3.400 | -0.302 |
| N2 | 57.00 | 3.200 | -0.324 |
| C4 | 30.70 | 3.600 | 0.06 |
| C5 | 30.70 | 3.600 | -0.17 |
| H2 | 12.00 | 0.500 | 0.32 |
| H3 | 25.45 | 2.360 | 0.117 |

Infinite Al(OH) rods



PZDC linkers



References

- (1) Lassitter, T.; Hanikel, N.; Coyle, D. J.; Hossain, M. I.; Lipinski, B.; O'Brien, M.; Hall, D. B.; Hastings, J.; Borja, J.; O'Neil, T.; Ephraim Neumann, S.; Moore, D. R.; Yaghi, O. M.; Grant Glover, T. Mass Transfer in Atmospheric Water Harvesting Systems. *Chem. Eng. Sci.* **2024**, *285*, 119430. <https://doi.org/10.1016/j.ces.2023.119430>.
- (2) Taler, D. Mathematical Models of Heat Exchangers. In *Numerical Modelling and Experimental Testing of Heat Exchangers*; Taler, D., Ed.; Studies in Systems, Decision and Control; Springer International Publishing: Cham, 2019; pp 321–337. https://doi.org/10.1007/978-3-319-91128-1_9.
- (3) Al Mesfer, M. K.; Danish, M. Breakthrough Adsorption Study of Activated Carbons for CO₂ Separation from Flue Gas. *J. Environ. Chem. Eng.* **2018**, *6* (4), 4514–4524. <https://doi.org/10.1016/j.jece.2018.06.042>.
- (4) Wilkins, N. S.; Rajendran, A.; Farooq, S. Dynamic Column Breakthrough Experiments for Measurement of Adsorption Equilibrium and Kinetics. *Adsorption* **2021**, *27* (3), 397–422. <https://doi.org/10.1007/s10450-020-00269-6>.
- (5) Silva, M. P.; Ribeiro, A. M.; Silva, C. G.; Nogueira, I. B. R.; Cho, K.-H.; Lee, U.-H.; Faria, J. L.; Loureiro, J. L.; Chang, J.-S.; Rodrigues, A. E.; Ferreira, A. MIL-160(Al) MOF's Potential in Adsorptive Water Harvesting. *Adsorption* **2021**, *27* (2), 213–226. <https://doi.org/10.1007/s10450-020-00286-5>.
- (6) Lyu, H.; Chen, O. I.-F.; Hanikel, N.; Hossain, M. I.; Flaig, R. W.; Pei, X.; Amin, A.; Doherty, M. D.; Impastato, R. K.; Glover, T. G.; Moore, D. R.; Yaghi, O. M. Carbon Dioxide Capture Chemistry of Amino Acid Functionalized Metal–Organic Frameworks in Humid Flue Gas. *J. Am. Chem. Soc.* **2022**, *144* (5), 2387–2396. <https://doi.org/10.1021/jacs.1c13368>.
- (7) Rajendran, A.; Shimizu, G. K. H.; Woo, T. K. The Challenge of Water Competition in Physical Adsorption of CO₂ by Porous Solids for Carbon Capture Applications – A Short Perspective. *Adv. Mater.* *n/a* (n/a), 2301730. <https://doi.org/10.1002/adma.202301730>.
- (8) Bozbiyik, B.; Van Assche, T.; Lannoe, J.; De Vos, D. E.; Baron, G. V.; Denayer, J. F. M. Stepped Water Isotherm and Breakthrough Curves on Aluminium Fumarate Metal–Organic Framework: Experimental and Modelling Study. *Adsorption* **2017**, *23* (1), 185–192. <https://doi.org/10.1007/s10450-016-9847-0>.
- (9) Grant Glover, T.; Peterson, G. W.; Schindler, B. J.; Britt, D.; Yaghi, O. MOF-74 Building Unit Has a Direct Impact on Toxic Gas Adsorption. *Chem. Eng. Sci.* **2011**, *66* (2), 163–170. <https://doi.org/10.1016/j.ces.2010.10.002>.
- (10) Rudisill, E. N.; Hacskeylo, J. J.; LeVan, M. D. Coadsorption of Hydrocarbons and Water on BPL Activated Carbon. *Ind. Eng. Chem. Res.* **1992**, *31* (4), 1122–1130. <https://doi.org/10.1021/ie00004a022>.
- (11) Sircar, S.; Mohr, R.; Ristic, C.; Rao, M. B. Isothermic Heat of Adsorption: Theory and Experiment. *J. Phys. Chem. B* **1999**, *103* (31), 6539–6546. <https://doi.org/10.1021/jp9903817>.
- (12) Pan, H.; Ritter, J. A.; Balbuena, P. B. Examination of the Approximations Used in Determining the Isothermic Heat of Adsorption from the Clausius–Clapeyron Equation. *Langmuir* **1998**, *14* (21), 6323–6327. <https://doi.org/10.1021/la9803373>.
- (13) Chheda, S.; Jeong, W.; Hanikel, N.; Gagliardi, L.; Siepmann, J. I. Monte Carlo Simulations of Water Adsorption in Aluminum Oxide Rod-Based Metal–Organic Frameworks. *J. Phys. Chem. C* **2023**, *127* (16), 7837–7851. <https://doi.org/10.1021/acs.jpcc.3c00354>.
- (14) Glover, T. G.; Wang, Y.; LeVan, M. D. Diffusion of Condensable Vapors in Single Adsorbent Particles Measured via Concentration-Swing Frequency Response. *Langmuir* **2008**, *24* (23), 13406–13413. <https://doi.org/10.1021/la802222r>.
- (15) Lassitter, T.; Hanikel, N.; Coyle, D. J.; Hossain, M. I.; Lipinski, B.; O'Brien, M.; Hall, D. B.; Hastings, J.; Borja, J.; O'Neil, T.; Ephraim Neumann, S.; Moore, D. R.; Yaghi, O. M.; Glover, T.G. Mass Transfer in Atmospheric Water Harvesting Systems. *Chem. Eng. Sci.* **2023**, 119430. <https://doi.org/10.1016/j.ces.2023.119430>.
- (16) Ruthven, D. M. *Principles of Adsorption and Adsorption Processes*; John Wiley & Sons, 1984.

- (17) Darken, L. S. Diffusion, Mobility and Their Interrelation through Free Energy in Binary Metallic System. *Trans. AIME Vol. 175, 1948*, 184–201.